RSC Advances

PAPER

View Article Online
View Journal | View Issue



Cite this: *RSC Adv.*, 2026, **16**, 2133

# Influence of molecular water dynamics on the electrical conductivity of hydrothermally synthesized hydroxyapatite from cuttlefish bone

Mariem Chaari, * Makram Megdiche and Mourad Arous

Hydrothermal transformation of natural aragonitic cuttlefish bones (Sepia officinalis) was used to successfully create hydroxyapatite nanoparticles ($Ca_{10}(PO_4)_6(OH)_2$), which were then completely studied using XRD, FTIR, and broadband dielectric spectroscopy (BDS). In this work, the electrical characteristics of hydroxyapatite are thoroughly examined throughout a wide frequency range (0.1 Hz to 1 MHz) and low temperature range (253 K to 473 K). While the DC conductivity shows characteristic non-Arrhenius behavior that is highly connected with thermal and spectroscopic investigations (FTIR, DSC, and TGA), the AC conductivity results show excellent agreement with both Almond-West formalism and Jonscher's universal power law. The dual conduction mechanisms controlled by the correlated barrier hopping (CBH) and non-overlapping small polaron tunneling (NSPT) models are confirmed by the temperature dependence of the frequency exponent *s*. Additionally, the AC conductivity data was used to extract important charge transport metrics, such as hopping energy, density of states at the Fermi level, and hopping distance. Deeper understanding of the intricate conduction pathways in hydroxyapatite is possible through the use of complementary impedance spectroscopy and Nyquist plot investigations. The crucial importance of charge carrier interactions and polaron dynamics in the conduction mechanism of biogenic hydroxyapatite is highlighted by this thorough electrical characterization, which paves the way for its optimal utilization in electronic and medicinal applications.

Received 18th October 2025
Accepted 21st December 2025

DOI: 10.1039/d5ra08000b

rsc.li/rsc-advances



## 1. Introduction

Apatites and apatite-based composites are a unique class of ceramics that have attracted a lot of interest because of their special structural and functional qualities. In biomedical study, these materials are especially pertinent since they closely mirror the inorganic components of human teeth and bone. In general, the term "apatites" refers to calcium phosphate compounds, of which hydroxyapatite (HAp), which has the chemical formula $[Ca_{10}(PO_4)_6(OH)_2]$, is an essential component. HAp is frequently utilized as a bone substitute in orthopedic and dental applications because of its exceptional biocompatibility, bioactivity, and osteoconductive properties.[1–3] Its usefulness also encompasses areas like environmental remediation[4] and energy storage.[5,6]

The polarization mechanisms of hydroxyapatite, an ionic crystal, are primarily controlled by hydroxyl ($OH^-$) ions.[7] With dipoles pointing perpendicular to each triangle's base, these $OH^-$ groups are positioned in the middle of equilateral triangles made up of surrounding $Ca^{2+}$ ions.[8] At different temperatures and frequencies, the dielectric and electrical behavior of HAp is strongly influenced by the orientation of these dipoles.[9] One of the main causes of the material's phase transitions is thought to be temperature-induced reorientation of $OH^-$ dipoles.[10] For example, A.K. Dubey *et al.* have proposed that the presence of $O_2$, $O^-$, and $OH^-$ species, as well as structural flaws produced during processing, affect the dielectric characteristics of HAp at low temperatures (below 423 K).[11] Polarization is also connected to the alignment of OH dipoles, which is linked to a phase transition at about 473 K from the monoclinic ($P2_1/b$) to the hexagonal ($P6_3/m$) structure.[10] This polarization tendency is also influenced by the displacement of hydroxyl ions.[12] At higher temperatures (>573 K), polarization is typically ascribed to the movement of thermally activated defects,[10] whereas Horiuchi *et al.* suggested that permanent polarization in HAp results from crystal defects in $OH^-$ sites.[9]

Electromagnetic fields are commonly used to promote bone regeneration and fracture repair since bone is a dielectric substance.[13,14] Biosensors can be made from HAp materials by adjusting their dielectric characteristics.[13,15] Furthermore, HAp coatings show promise for use in electrical insulation, especially for electronic devices that are implanted.[13,16]

*In vitro* and *in vivo* crystallization of inorganic ions has also been demonstrated to be significantly influenced by the surface charge of HAp.[2,17] Positively charged surfaces tend to impede bone formation, whereas negatively charged surfaces seem to

*Laboratory of Ceramics, Composites and Polymers Materials (LaMaCoP), Faculty of Sciences of Sfax, University of Sfax, 3018 Sfax, Tunisia. E-mail: mariem.chaari@fss.usf.tn*

promote it.[18] The significance of surface charge in biological response was further highlighted by a more recent study by Nakamura *et al.*,[19] which found that both positive and negative charges encourage cytoskeletal rearrangement in osteoblast-like cells.

At low temperatures (below 473 K), we present a novel technique in this work to calculate the activation energy for ionic conduction in hydroxyapatite. The goal of this method is to determine the type of mobile charge carriers that contribute to conduction. As far as we are aware, no other study has methodically investigated the DC and AC electrical conductivity of HAp powders that display non-Arrhenius behavior, especially when exposed to water at low temperatures. Clarifying how water affects the electrical energy landscape of HAp materials requires an understanding of this interaction.

## 2. Experimental

### 2.1. Synthesis of hydroxyapatite (HA) powder

Calcium carbonate ($CaCO_3$) was extracted from the lamellar portion of cuttlefish bone to start the formation of hydroxyapatite (HAp). Prior to being pounded into a fine powder with a mortar, the extracted material was first calcined in a furnace at 350 °C for three hours to remove the organic matter while preserving the aragonite structure of the cuttlefish bone.[20]

A 1 M $CaCO_3$ solution was made by dissolving 10 g of the resultant $CaCO_3$ powder in 100 mL of distilled water in order to create the HA. Concurrently, 6.9 g of ammonium dihydrogen phosphate ($NH_4H_2PO_4$) was dissolved in 100 mL of distilled water to create a 0.4 M solution. The following equation represents the overall reaction that leads to the creation of HAp:

$$10CaCO_3 + 6NH_4H_2PO_4 + 2H_2O \rightarrow Ca_{10}(PO_4)_6(OH)_2 + 3(NH_4)_2CO_3 + 7CO_2 + 7H_2O \quad (1)$$

After 30 minutes of continuous magnetic stirring, the 1 M $CaCO_3$ solution was combined with the $NH_4H_2PO_4$ solution. The resultant slurry was put into a stainless-steel autoclave lined with Teflon and hydrothermally treated for 12 hours at 200 °C in a lab oven. The autoclave was allowed to gradually drop to ambient temperature following the process. To get rid of any remaining acidic byproducts, the precipitate was gathered and carefully cleaned with distilled water. Until the pH was balanced, washing was continued. To stop the HAp particles from clumping together during the drying process, a final rinse with analytical-grade methanol was performed. After passing through filter paper, the purified precipitate was dried in an electric oven set at 50 °C for an hour. The dry HAp powder was then sintered in a furnace for an hour at 900 °C. To create a fine, uniform HAp powder that could be used for characterization, the sintered material was next ground for nine hours at 500 rpm using a zirconium milling jar filled with zirconium balls.

### 2.2. Material characterization

X-ray diffraction (XRD) was used to characterize the produced powder's structure. Using an X'Pert3 Powder Panalytical diffractometer running at 40 mA and 45 kV with Cu $K\alpha_1$ radiation ($\lambda = 1.54059$ Å), the diffraction patterns were captured throughout a $2\theta$ range of 10° to 70°.

Using a PerkinElmer Pyris 4000 system, Differential Scanning Calorimetry (DSC) was used to study thermal behavior. Under a nitrogen environment, measurements were carried out between −20 °C and 300 °C at a steady heating rate of 5 °C $min^{-1}$.

Using thermogravimetric analysis (TGA) and a PerkinElmer TGA 400 equipment, the sample's thermal stability was assessed. Under a nitrogen flow, measurements were made between 298 K and 873 K (corresponding to 25 and 600 °C at a heating rate of 10 °C $min^{-1}$).

Bonding environments and functional groups were identified using Fourier Transform Infrared (FT-IR) spectroscopy. A PerkinElmer Spectrum spectrometer (Waltham, MA, USA) was used to record the spectra at room temperature, covering the 500–4000 $cm^{-1}$ spectral range.

The HA powder was uniaxially crushed into pellets with a diameter of 10 mm and a thickness of roughly 0.83 mm in order to perform dielectric and electrical characterization. A Novocontrol Broadband Dielectric Spectroscopy (BDS) equipment (Novocontrol Technologies GmbH & Co. KG) was used to do the tests. It operated between 253 K and 474 K in temperature and between 0.1 Hz and 1 MHz in frequency. The sample temperature was controlled using a regulated nitrogen flow. The pellets were positioned between two 24 mm-diameter, parallel, gold-plated electrodes. An alternating electric field was created by applying a 1 V alternating sinusoidal voltage perpendicular to the pellet surfaces. Dielectric relaxation events are characterized by polarization responses, such as oscillations at the same frequency as the applied field but with a phase shift between the voltage and current signals.

## 3. Results and discussion

### 3.1. XRD analysis

X-ray diffraction (XRD) was used to analyze the phase composition and structural properties of the produced hydroxyapatite (HA) powder. The FullProf program was used to perform Rietveld refinement analysis on the room temperature diffraction pattern seen in Fig. 1.

The indexing of all significant peaks indicates that the primary phase is hydroxyapatite $Ca_{10}(PO_4)_6(OH)_2$, which has hexagonal symmetry (space group $P6_3/m$). The improved lattice parameters, $a = 9.42320$ Å and $c = 6.88515$ Å, were found to be in agreement with the values reported in the literature for stoichiometric HA.

A low-intensity peak in the diffractogram indicated the presence of a small impurity that corresponded to β-tricalcium phosphate (β-TCP). Its existence could be explained by insufficient reactions during the synthesis process or minute variations in the Ca/P molar ratio.

To evaluate the microstructural quality of the HA powder, the average crystallite size $D_{hkl}$ was estimated using the Debye–Scherrer equation:[21,22]

$$D_{hkl} = \frac{K\lambda}{\beta \cos\theta} \quad (2)$$

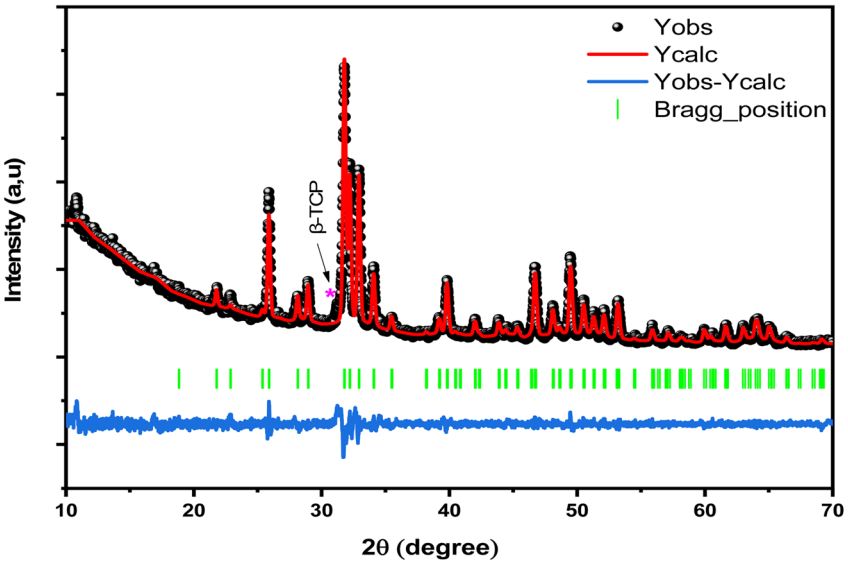


Fig. 1 XRD pattern of the synthesized hydroxyapatite (HAp) powder.

where $\lambda = 1.54059$ Å (Cu K$\alpha_1$), $K = 0.89$, $\beta$ is the full width at half maximum (FWHM) of selected reflections, and $\theta$ indicates the peak XRD position.

The analysis was based on the most intense and well-defined diffraction peaks at $2\theta$ = 25.85°, 31.76°, 32.17°, and 32.89°, corresponding to the (002), (211), (112), and (003) planes, respectively. The sharpness of these peaks reflects a high degree of crystallinity.

The degree of crystallinity $\chi_c$, which quantifies the proportion of crystalline phase in the sample, was calculated using two complementary approaches:

Empirical intensity-based method:[23]

$$\chi_c = 1 - \frac{\nu_{112/003}}{I_{003}} \quad (3)$$

where $I_{003}$ is the intensity of (003) diffraction peak and $\nu_{112/030}$ the intensity of the hollow between (112) and (003) diffraction peaks of HAp.

Crystallite-size-based method, which accounts for peak broadening:[23]

$$\chi_c = \left(\frac{K'}{\beta_{002}}\right)^{0.33} \quad (4)$$

with $K' = 0.24$, and $\beta_{002}$ being the FWHM of the (002) reflection.

The average crystallite size, as shown in Table 1, is roughly 33.92 nm, which is within the anticipated nanometric range for hydroxyapatite produced by hydrothermal or wet chemical methods.

The crystallinity of the hydroxyapatite sample was evaluated using the peak intensity method (eqn (3)), where the (003) reflection was chosen as the reference crystalline peak. Using this approach, the crystallinity was calculated as 0.73 (73%), consistent with the broad amorphous halo observed between $2\theta$ = 30–40°. In comparison, the empirical relation based on the (002) peak width,(eqn (4)), gave a value slightly above 1 (1.01), overestimating crystallinity as it reflects crystallite size and structural perfection rather than the amorphous fraction. Therefore, the peak intensity method (eqn (3)) provides a more realistic estimation of the actual crystallinity. Because it frequently correlates with better mechanical stability and slower rates of dissolution under physiological settings, such high crystallinity is advantageous for biomedical applications.

### 3.2. FTIR results

The synthesis of HAp is confirmed by the FTIR spectra of the produced hydroxyapatite (Fig. 2), which shows the distinctive absorption bands linked to phosphate groups ($PO_4^{3-}$) at 1087, 1018, 965, 594, and 555 $cm^{-1}$.[24]

The presence of adsorbed water molecules, which are normally kept on the powder surface during synthesis, is indicated by a broad absorption band with a center at 3422 $cm^{-1}$ and a narrower bending vibration at 1639 $cm^{-1}$.[25,26] The vibrational modes of carbonate ions ($CO_3^{2-}$) are responsible for additional absorption peaks detected at 1458, 1412, and 877 $cm^{-1}$.[27] The partial substitution of carbonate ions into the apatite lattice, which is frequently seen in biological apatites, is reflected in these bands.

In HAp, carbonate substitution can take two forms: A-type, in which $OH^-$ groups are replaced by $CO_3^{2-}$, and B-type, in which $PO_4^{3-}$ groups are replaced.[28,29] The characteristic doublets and the peak at 877 $cm^{-1}$ in the FTIR spectrum demonstrate the

Table 1 Average crystallite size ($D$) and crystallinity degree ($\chi_c$) of the synthesized hydroxyapatite

| | |
|---|---|
| Mean crystallite size. $D$ (nm) | 33.92 |
| Crystallinity. $\chi_c$ eqn (3) | 0.73 |
| Crystallinity. $\chi_c$ eqn (4) | 1.01 |

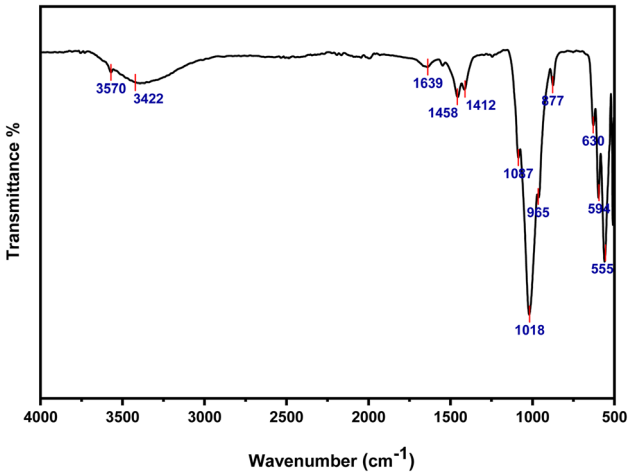


Fig. 2 FT-IR spectrum of synthesized hydroxyapatite (HAp).

existence of both kinds of substitutions. Instead of being completely removed during thermal processing, these carbonate-associated bands imply that ambient $CO_2$ might have been integrated into the HAp lattice during synthesis.[30] Since carbonated apatites closely resemble the mineral phase of normal bone and improve biological performance, adding $CO_3^{2-}$ ions is frequently advantageous for bioactivity rather than harmful.[31] Additionally, the vibrational modes of the hydroxyl ($OH^-$) groups found in the HAp structure are represented by the bands seen at 3570 $cm^{-1}$ (stretching) and 630 $cm^{-1}$ (bending).[30,32,33] These $OH^-$ bands' comparatively low intensity is characteristic of nanocrystalline biological apatites, where a decrease in $OH^-$ content is frequently caused by enhanced carbonate ion replacement.[34]

### 3.3. DSC analysis

Fig. 3(a and b) displays the synthesised hydroxyapatite (HAp) sample's differential scanning calorimetry (DSC) thermogram. Fig. 3(a) presents the complete thermal program, which includes three successive steps: an initial heating, a cooling phase, and a second heating cycle. Particular attention is paid to the initial heating run in Fig. 3(b). The purpose of this DSC investigation was to find possible thermal events, such as phase changes, endothermic or exothermic transitions, or thermal impacts associated with moisture release.

Interestingly, neither the cooling phase nor the second heating cycle showed any notable thermal events, as seen in Fig. 3(a). This demonstrates the material's thermal stability and implies that the first peak results from the removal of surface water that is weakly bound and only exists before the initial heating. The conclusion that the observed endothermic shift is caused by the desorption of remaining moisture rather than a structural phase transition is supported by the lack of additional thermal changes in succeeding cycles.

The first heating cycle exhibits a noticeable endothermic peak with a maximum temperature ($T_{Max}$) of 343.23 K (matching to 70.23 °C as shown in the DSC curve) and a corresponding enthalpy change ($\Delta H$) of 80.46 J $g^{-1}$, as seen in Fig. 3(b). This

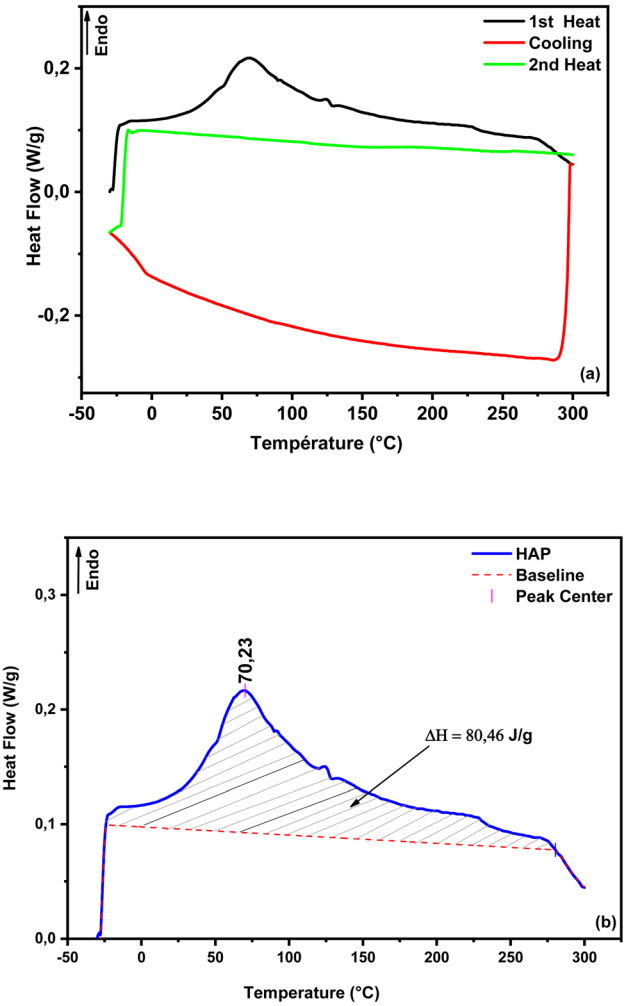


Fig. 3 (a and b) Differential scanning calorimetry (DSC) analysis of the synthesized hydroxyapatite (HAp).

heat response is in line with the findings of Irfan *et al.*,[35] who found that HAp made from fish bones and mussel shells had a comparable peak at about 343 K. This endothermic event is explained by the release of physically adsorbed water from the surface and porous structure of the HAp particles, which is a feature frequently seen in nanostructured or biologically derived apatites that have a tendency to absorb ambient moisture, according to FTIR results and data from the literature.

### 3.4. ATG results

The thermogravimetric analysis (TGA) of the produced HAP powder is displayed in Fig. 4.

In addition to offering information about the sample's thermal stability, the measured mass losses could also be a reflection of sublimation, vaporization, or chemical breakdown at high temperatures. A 3% mass loss is seen when heated to about 873 K, which is probably caused by the partial removal of chemically and physically adsorbed water as well as potential lattice water. This conclusion is in line with the DSC and IR findings. Between 298 and 473 K, adsorbed water is progressively eliminated without changing the crystal structure.[36]

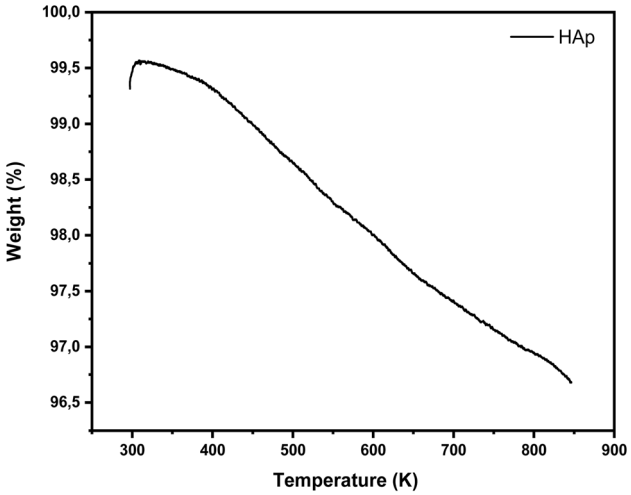


Fig. 4 Variation of the sample mass percentage as a function of temperature, based on the thermogravimetric analysis of HAp powder.

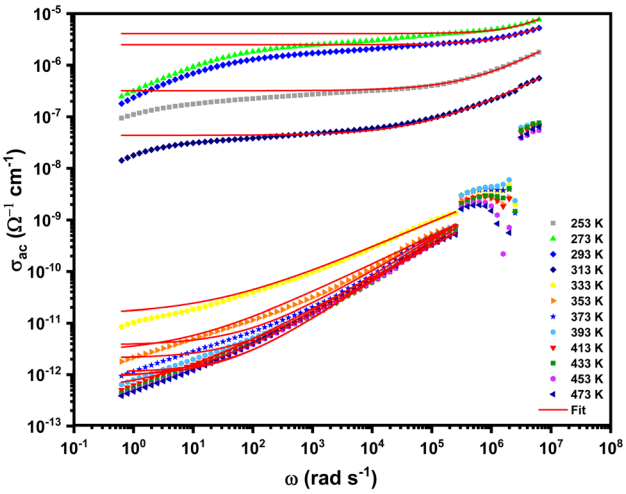


Fig. 5 Frequency dependence of the AC conductivity at various temperatures for the prepared HAp. The solid lines represent the best nonlinear fits of the experimental data using Jonscher's law and the Almond-West model.

It exists in two layers: an inner layer that needs greater temperatures to be released and an exterior layer that evaporates readily. Even higher temperatures are needed to remove water that has been retained by adhesion and cohesion forces in tiny areas like pores and fissures. The crystal shrinks slightly between 473 K and 673 K due to the irreversible loss of lattice water, which is a component of the crystal structure itself.[37] Phosphorus on the surface interacts to create new chemical bonds (P–O–P groups) at temperatures above 673 K.[38]

### 3.5. DC conductivity analysis

The real component of the AC conductivity ($\sigma_{ac}$) as a function of frequency at different temperatures, as seen in Fig. 5.

According to the Almond-West model,[39] the synthesized HAP powder's AC conductivity behavior exhibits a power-law relationship:

$$\sigma_{ac}(\omega) = \sigma_{dc}\left[1 + \left(\frac{\omega}{\omega_H}\right)^n\right] \quad (5)$$

Due to space charge accumulation at the blocking electrodes, interfacial polarization effects at the electrode–sample interface are responsible for the noticeable spike seen at very low frequencies.[40] A frequency-independent plateau that represents the material's DC conductivity ($\sigma_{dc}$) appears after this spike. In this case, $n$ is the frequency exponent, and $\omega_H$ is the hopping frequency that indicates the change from the frequency-independent (DC) to the dispersive (AC) zone. As indicated by the solid lines in Fig. 5, the parameters $\sigma_{dc}$, $\omega_H$, and $n$ were recovered by fitting the conductivity spectra with a nonlinear curve using eqn (5).

In parallel, the conductivity spectra ($\sigma_{ac}(\omega)$) also obey Jonscher's universal power law:[41]

$$\sigma_{ac} = \sigma_{dc} + A\omega^S \quad (6)$$

where $\sigma_{dc}$ is the low-frequency (DC) conductivity, $A$ is a temperature-dependent pre-exponential factor, $\omega$ is the angular frequency, and $s$ is the frequency exponent that characterizes the interaction between mobile charge carriers and the lattice environment. It is observed that $s$ varies with temperature.

Using eqn (6), the experimental data was nonlinearly fitted to yield the parameters $\sigma_{dc}$, $A$, and $s$. Fig. 5 displays the fitted curves. Important details about the conduction mechanism are revealed by the exponent $s$: translational hopping dominates charge transport when $s < 1$, while localization predominates when $s > 1$. Notably, the $\sigma_{dc}$ values obtained from the Almond-West and Jonscher models correspond well, and the values of $s$ nearly resemble those of $n$.

As illustrated in Fig. 5, DC conductivity first increases with temperature and peaks at 278 K. After this temperature, $\sigma_{dc}$ steadily drops. Water desorption from the HAp surface is probably the cause of this decrease in surface conduction. The literature has documented similar patterns. From ambient temperature to 473 K, Gittings *et al.* found that conductivity decreased. They attributed this to the dehydration of hydroxyapatite and the loss of surface-bound water.[42] When heated to 923 K, Roy *et al.*[43] similarly discovered decreased conductivity in HAp, which they attributed to the loss of structural water. Water released up to 573 K is thought to contain both weakly and highly physisorbed water, according to Nagai and Nishino.[44] The spectra show a discernible change in AC conductivity at higher frequencies (see Fig. 5), especially at temperatures greater than 278 K. Water evaporation at the interfaces between the gold electrodes, HAp, and nitrogen, areas likewise thought to be active sites for $H_2O$ dissociation, is thought to be the cause of this abrupt shift in conductivity. Yamashita *et al.*,[45] who looked into how conductivity is affected by time-dependent instability and dehydration behavior, discovered a similar occurrence.

### 3.6 Investigation of activation energies from $\sigma_{dc}$ and $\omega_H$ (Almond-West) with non-Arrhenius temperature dependence

In order to determine the activation energy governing the DC conductivity process and its temperature-dependent behavior,

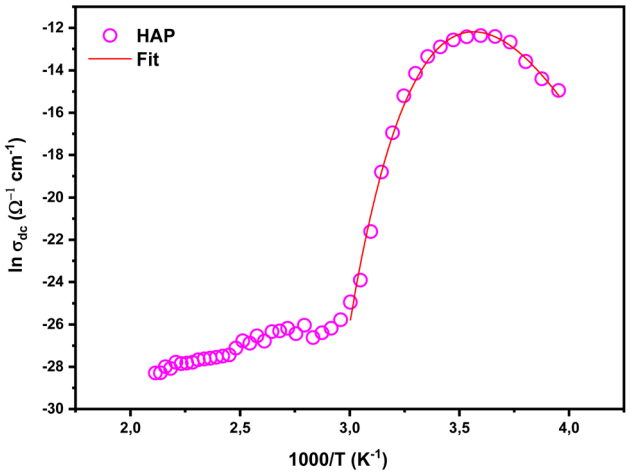


Fig. 6 Logarithmic plot of DC conductivity ($\sigma_{dc}$) *versus* inverse temperature for the prepared HA powder. The solid lines represent the best-fit curves obtained using eqn (6).

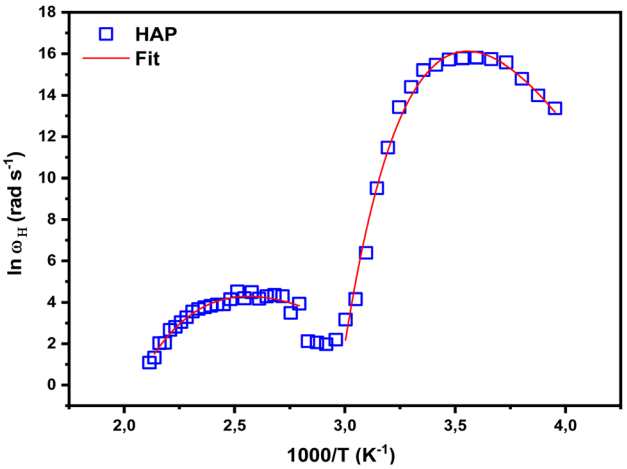


Fig. 7 Plot of log $\omega_H$ *versus* the reciprocal of temperature (1000/*T*) for the prepared HA powder. The solid lines represent the best-fit curves obtained using eqn (7).

the DC conductivity values $\sigma_{dc}$ extracted from the Jonscher fitting were plotted as a function of the absolute temperature. The DC conductivity logarithmic curve as a function of the inverse of absolute temperature is shown in Fig. 6. This analysis allows identification of the different contributions to the conduction mechanisms and quantification of the energy required for charge carrier motion, taking into account the non-Arrhenius temperature dependence observed.

In contrast to typical Arrhenius behavior, the experimental data form an inverted saddle-shaped curve with a local maximum. Gittings *et al.*[42] discovered similar conductivity patterns in hydroxyapatite at low frequencies (1 Hz) and temperatures below 473 K. They ascribed the observed behavior to the loss of surface-bound water. Tanaka *et al.*[46] also noted that the conductivity of hydroxyapatite powders and whiskers showed a nonlinear temperature relationship. They proposed that the competing effects of increased and decreased conduction routes associated with adsorbed water are the cause of this nonlinearity, especially below 523 K. According to earlier research,[47–50] this kind of non-Arrhenius behavior usually results from either a loss of some degrees of freedom for ion diffusion as the temperature drops or from improved cooperative dynamics among charge carriers. On the basis of this assumption, a model based on Macedo and Litovitz's theoretical framework was used to fit the experimental data.[51] Douiri *et al.*[52] showed in a comparable context that dielectric water relaxations in geopolymers across wide temperature ranges follow a similar methodology based on the Macedo–Litovitz model. According to this concept, DC conductivity is controlled by two simultaneous processes: (a) molecules must cross a specific energy threshold in order to reorient themselves, and (b) there must be a nearby defect site with enough free volume to permit this reorientation.

Within this theoretical framework, the temperature dependence of DC conductivity is described by the following equation:

$$\sigma_{dc} = \sigma_0 \exp\left[-\left(\frac{E_{dc(a)}}{K_B T} + C\ \exp\left(-\frac{E_{dc(b)}}{K_B T}\right)\right)\right] \quad (7)$$

In this expression, $\sigma_0$ is a pre-exponential conductivity factor,[53] $C \sim 1/\eta$, where $\eta$ indicates the highest feasible concentration of defects, $E_{dc(a)}$ is the energy barrier between equilibrium locations, and $E_{dc(b)}$ is the energy necessary for defect production. Table 2 shows the hydroxyapatite's fitted activation energy values, $E_{dc(a)}$ and $E_{dc(b)}$.

A similar conductivity trend was also discovered by Gittings *et al.*,[42] but they only examined the Arrhenius zone, which is between 973 and 1273 K. They calculated activation energies between 1.86 and 2.23 eV. The activation energy $E_{dc(a)}$ of our

Table 2 Fitting parameters obtained from eqn (7). Eqn (8) and (12)

| $\ln \sigma_{dc} = f\left(\frac{1000}{T}\right)$ | | $\ln \omega_H = f\left(\frac{1000}{T}\right)$ | | | $\ln \tau = f\left(\frac{1000}{T}\right)$ | | $\ln \tau = f\left(\frac{1000}{T}\right)$ | |
|---|---|---|---|---|---|---|---|---|
| | | | Higher pic. | Lower pic. | | | | |
| $E_{dc(a)}$ (eV) | 1.93 | $E_{H(a)}$ (eV) | 1.64 | 0.69 | $E_a$ (eV) | 1.89 | $E_{R(a)}$ (eV) | 1.82 |
| $E_{dc(b)}$ (eV) | 0.20 | $E_{H(b)}$ (eV) | 0.23 | 0.22 | $E_b$ (eV) | 0.20 | $E_{R(b)}$ (eV) | 0.22 |
| ln $\sigma_0$ | 77.26 | ln $\omega_0$ | 90.86 | 28.03 | ln $\tau_0$ | −103.49 | ln $\tau_0$ | −73.02 |
| *C* | 41 976.12 | *C* | 110 988.26 | 2228.72 | *C* | 40 744.47 | *C* | 86 046.37 |

synthesized HAp is further confirmed by theoretical studies[54–56] to be in agreement with values related to $OH^-$ ion hopping along the *c*-axis in hexagonal crystal formations. This implies that the primary charge carriers in charge of conductivity in the measured frequency range are probably $OH^-$ ions.

To determine the activation energy of the high-frequency conductivity process, $\omega_H$ values extracted from the Almond-West fitting were used to analyze the temperature-dependent AC conductivity (short-range hopping) and to compare it with DC conductivity, which reflects long-range hopping. We investigated the logarithmic change of the hopping frequency ($\omega_H$) as a function of the inverse temperature in order to calculate the free energy related to ion migration. This relationship, which is shown in Fig. 7, adheres to the extended model given by eqn (8) rather than the standard Arrhenius behavior:

$$\ln R_1 = f\left(\frac{1000}{T}\right) \tag{8}$$

Here, $E_H$ stands for the energy needed for polaron movement, also known as the migration free energy of mobile ions, and $\omega_0$ is the effective attempt frequency.[53]

Comparison of Fig. 6 and 7 shows that at low temperatures, both $\sigma_{dc}$ and $\omega_H$ exhibit pronounced peaks due to water-assisted hopping. As the temperature increases, the desorption of adsorbed water disrupts long-range conduction pathways, reducing $\sigma_{dc}$, while $\omega_H$ continues to reflect short-range hopping, producing a small but still visible peak. This behavior also accounts for the observed non-Arrhenius temperature dependence.

Table 2 reports the activation energies $E_{H(a)}$ and $E_{H(b)}$, which were determined by fitting the experimental data with the Macedo–Litovitz model.[51] The temperature dependence of $\omega_H$ revealed two different activation energies: 1.64 eV (denoted $E_{H_2(a)}$) for temperatures below 333 K and 0.69 eV (denoted $E_{H_1(a)}$) for temperatures above 333 K. The reorientation of $OH^-$ ions is responsible for the first value, 0.69 eV. This result is in line with findings from Horuichi *et al.*,[57] who used thermally stimulated depolarization current (TSDC) measurements to report the same activation energy. Dipolar polarization, which results from the alignment of $OH^-$ ions into a polar phase inside the crystal structure, was linked to it. The 1.5 eV value that Royce[55] previously attributed to $O_2^-$ ion conduction in hydroxyapatite is equivalent to the second activation energy of 1.64 eV. Furthermore, it is significant to notice that the activation energies $E_{dc(b)}$ and $E_{H(b)}$ are almost the same, lying between 0.20 and 0.23 eV. This resemblance implies that both could be protonic charge carriers produced *via* $OH^-$ vacancy generation. According to Yamashita *et al.*,[45] protons liberated during dehydration move through hydroxyapatite following routes delineated by the ionic groups $PO_4^{3-}$ and $OH^-$.

In conclusion, charge transport at low temperatures (below 373 K) is significantly influenced by proton migration in adsorbed water layers on the surface of hydroxyapatite (HAp).[42] When the temperature rises, the kinetic energy involved is enough to drive water molecules out of internal channels, mostly *via* *c*-axis-aligned crystallite terminations. Complete dehydration is challenging and takes time over a wide temperature range because water molecules farther inside the crystallite need more energy to be extracted than those closer to the surface. Structural water removal requires more energy than bulk or loosely linked water because of the stronger hydrogen bonds and charge–dipole interactions seen in solid hydroxyapatite. Heating promotes water desorption because the balance between structural and bulk water is temperature-dependent and controlled by enthalpy changes. The endpoints of the *c*-axis are probably where water molecules move in and out. They might migrate *via* proton transfer to nearby hydroxide ions along *c*-axis channels at higher temperatures. Water is expelled at the channel termini as a result of this action, and the amount of hydroxide ions inside the channels rises.[58]

### 3.7. Dielectric analysis

Understanding hydroxyapatite's (HAp) dielectric characteristics is essential to understanding how it conducts protons. This study examined the dielectric response by analyzing the complex electric modulus ($M^*$) and the complex dielectric constant ($\varepsilon^*$) as functions of temperature and frequency. The following relations were used to compute these parameters from the measured complex impedance ($Z^*$):

$$\omega_H = \omega_0 \exp\left[-\left(\frac{E_{H(a)}}{K_B T} + C \exp\left(-\frac{E_{H(b)}}{K_B T}\right)\right)\right] \tag{9}$$

$$\varepsilon^* = \varepsilon' - i\varepsilon'' = \left(\frac{-Z''}{\omega C_0\left(Z'^2 + Z''^2\right)}\right) - i\left(\frac{Z'}{\omega C_0\left(Z'^2 + Z''^2\right)}\right) \tag{10}$$

**3.7.1. Real part of the dielectric constant ($\varepsilon'$).** The real component of the dielectric constant ($\varepsilon'$) varies with frequency at different temperatures, as shown in Fig. 8.

The material's electrical energy storage capacity and the degree of dipole alignment in response to an external electric

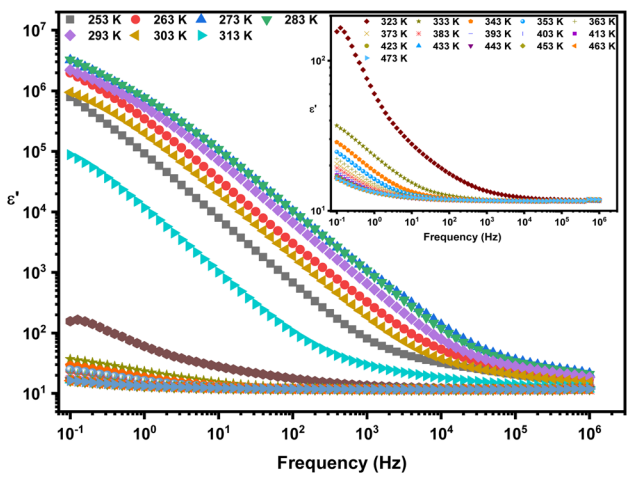


Fig. 8 Frequency dependence of the real part of the relative permittivity ($\varepsilon'$) at various temperatures for the prepared HAp.

field are both described by the parameter $\varepsilon'$. As the frequency rises, $\varepsilon'$ is seen to significantly drop. $\varepsilon'$ shows high values at low frequencies and gradually decreases as the frequency rises. This phenomenon is explained by dipoles' limited capacity to rapidly reorient in order to track the applied AC field's fast oscillations at higher frequencies.

Ionic species including $Ca^{2+}$, $PO_4^{3-}$, and $OH^-$ make up the structure of HAp and form channels along the *c*-axis. Because of their orientational polarization, $OH^-$ dipoles among these contribute significantly to the dielectric constant, but the contributions of other ions are comparatively small. Because the oscillating electric field resonates with the $OH^-$ dipoles' inherent response frequency at low frequencies, both electronic and ionic polarization mechanisms are activated, resulting in a large $\varepsilon'$. On the other hand, the dipoles are unable to reorient quickly enough at high frequencies, which results in less polarization and a decrease in $\varepsilon'$.

From 253 K to 278 K, $\varepsilon'$ rises in the low-frequency zone; at higher temperatures, it falls. $\varepsilon'$ stays much higher in this temperature range, from $4 \times 10^6$ to $1 \times 10^5$, before dropping off rapidly from 323 K onward, reaching values of about 20 at 473 K. This pattern is consistent with the change in DC conductivity with temperature, suggesting that the loss of surface-bound water and dehydration of the HAp structure are the likely causes of the drop in $\varepsilon'$ at high temperatures. In contrast to denser materials, Gittings *et al.*[42] showed that porous HAp sintered in water vapor had increased permittivity because of improved conductivity, especially at low frequencies and below 523 K. Likewise, Roy *et al.*[43] found that higher ambient humidity increased permittivity, which they attributed to better proton conduction.

**3.7.2. Imaginary part of the dielectric constant ($\varepsilon''$).** The imaginary component of the dielectric constant ($\varepsilon''$) as a function of frequency is shown in Fig. 9.

Like $\varepsilon'$, the $\varepsilon''$ values show a trend of high values at low frequencies. Large interfacial capacitance and ionic charge accumulation at the HAp/electrode interface[59] are to blame for this, as they also increase the area's capacity for energy dissipation and storage. The material's energy dissipation mechanisms, such as interfacial polarization, ionic conduction, and dipolar relaxation, are actually reflected in the imaginary component of the dielectric permittivity ($\varepsilon''$).

**3.7.3. Electric modulus analysis ($M''$).** The imaginary part of the electric modulus ($M''$), shown in Fig. 10, provides a useful representation in solid dielectric materials, as it reduces the effects of electrode polarization (EP) at low frequencies.

Additionally, $M''$ is indifferent to surface contaminants, contact flaws, and electrode characteristics.[59,60] Non-Debye-type conductivity relaxation is shown by the wide relaxation peaks in the $M''$ spectra. The temperature increases from 253 K to 283 K, causing these peaks to move toward higher frequencies. But as the temperature rises above this range, they return to lower frequencies. This change points to a thermally triggered change from short-range to long-range ion mobility: heavy and less mobile ions move between lattice sites through hopping mechanisms at low frequencies, but they stay trapped in local potential wells at high frequencies, only moving locally.[61]

**3.7.4. Activation energy from dielectric relaxation.** The characteristic relaxation time ($\tau$) associated with $M''$ is calculated using the peak frequency $f_{p(M'')}$ according to:

$$M^* = M' + iM'' = \frac{\varepsilon'}{\varepsilon'^2 + \varepsilon''^2} + i\frac{\varepsilon''}{\varepsilon'^2 + \varepsilon''^2} \quad (11)$$

Fig. 11 plots the temperature dependence of $\tau$ to calculate the activation energy of the relaxation process.

Non-Arrhenius behavior is indicated by the saddle-like curve formed by the resultant data. The Macedo–Litovitz model,[51] which has also been used in dielectric relaxation studies of water in geopolymers,[52] was thus used to fit the data.

This model indicates that the relaxation time's temperature dependence is as follows:

$$\tau = \frac{1}{2\pi f_{p(M'')}} \quad (12)$$

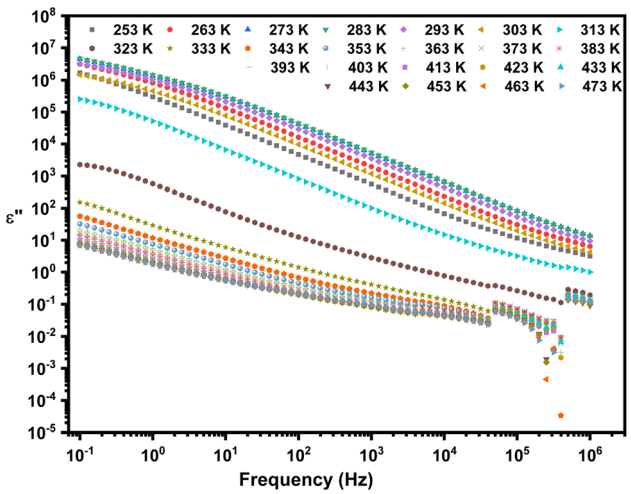


Fig. 9 Frequency dependence of the imaginary part of the permittivity ($\varepsilon''$) at various temperatures for the prepared Hap.

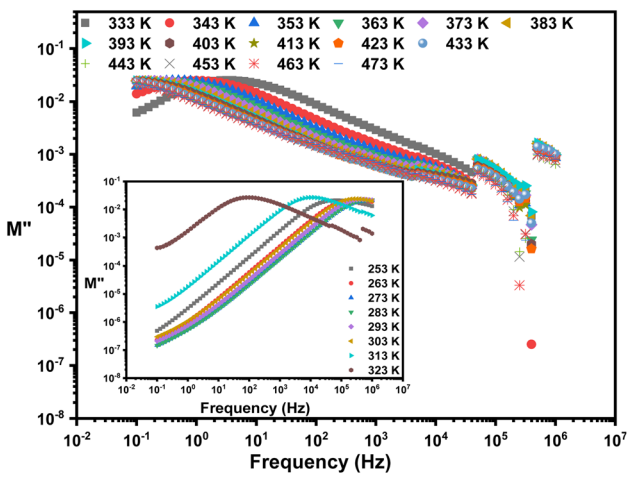


Fig. 10 Frequency dependence of the imaginary part of the electric modulus ($M''$) at various temperatures for the prepared HAp.

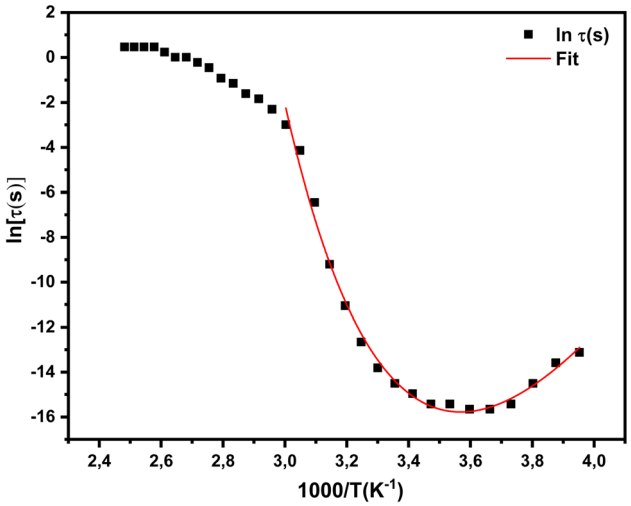


Fig. 11 Temperature dependence of the relaxation time $\tau$ for the prepared HAp.

where $E_a$ is the potential barrier height between equilibrium states, $E_b$ is the defect formation energy, and $C \sim 1/\eta$, with $\eta$ being the maximum defect concentration. The fitted activation energies $E_a$ and $E_b$ for the hydroxyapatite sample are listed in Table 2. Notably, the obtained energy values are very similar to those derived from DC conductivity measurements, suggesting a consistent conduction mechanism across both electrical and dielectric responses.

### 3.8. Theoretical exploration of the conduction mechanism

Fig. 12 displays the temperature dependence of the frequency exponent $s$, revealing four distinct regions. In regions (I) and (II), $s$ increases with temperature, whereas in regions (III) and (IV), it decreases as the temperature continues to rise.

Fig. 13 shows the ratio of $-\log_{10}A/s$ as a function of temperature to help explore the conduction mechanism further.

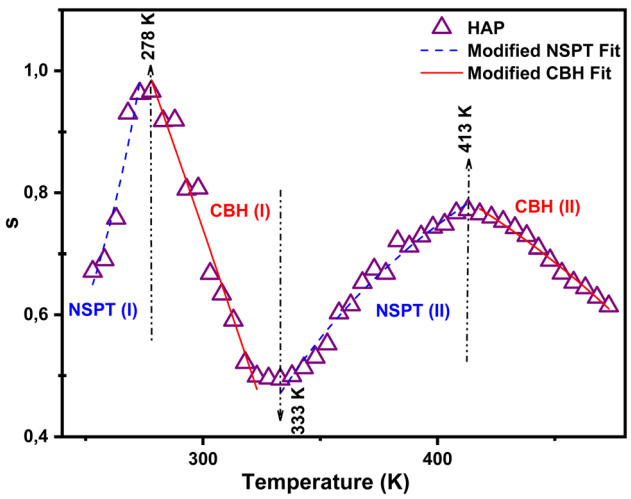


Fig. 12 Temperature dependence of the frequency exponent s for the prepared HAp.

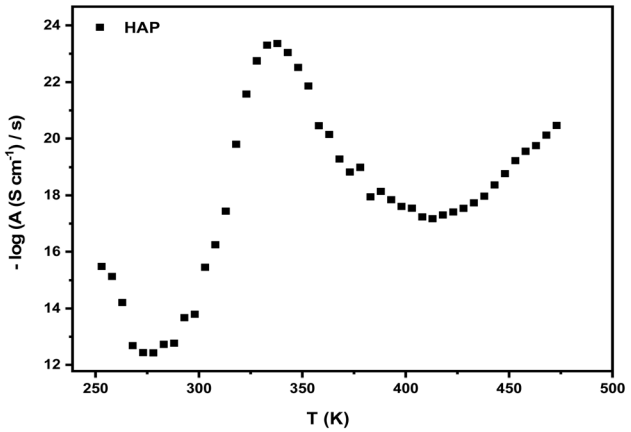


Fig. 13 The variation of the ratio of $-\log(A/s)$ as functions of temperature for the prepared HAp.

Given that this ratio is not constant, it can be inferred that a hopping mechanism most likely governs the conduction process because the temperature dependence of $-\log_{10}A/s$ differs from that of $s$. The inherent characteristics of the material and its microstructural network frequently influence the association between $\log_{10}A$ and $s$.[62]

The temperature dependence of $s(T)$ and the AC conduction mechanism have been explained by a number of theoretical theories, including:

In the overlapping large polaron tunneling (OLPT) model, the parameter $s$ first falls to a minimum as the temperature rises, and then it rises once more.[63]

The exponent $s$ rises with temperature in the nonoverlapping small polaron tunneling (NSPT) model, which is consistent with the patterns observed in areas I and III.[64]

Correlated barrier hopping (CBH) model: in line with findings in areas II and IV, the exponent $s$ decreases with temperature.[65]

The exponent $s$ in the quantum mechanical tunneling (QMT) model is either very constant ($\sim$0.8) or just slightly changes with temperature.[66]

**3.8.1. Non-overlapping small polaron tunneling (NSPT) model analysis.** The phenomena of small polarons moving between isolated places in a material without overlapping or interacting with adjacent polarons is described by the Nonoverlapping Small Polaron Tunneling (NSPT) model, which is based on the literature.[67] Grasp charge conduction in some materials with disordered structures requires a grasp of this paradigm. The following formula[68] can be used to get the exponent "$s$" in the NSPT model:

$$\tau = \tau_0 \exp\left(\frac{E_a}{K_B T} + C \exp\left(-\frac{E_b}{K_B T}\right)\right) \quad (13)$$

The activation energy for particle transfer ($W_H$) in the nonoverlapping small polaron tunneling (NSPT) model is independent of site spacing, and the distortions around two sites do not overlap.[68] The experimental findings are not sufficiently consistent with the NSPT concept. As a result,

modifications have been made to enhance the experimental results. The nonoverlapping small polaron tunneling (NSPT) model's modified equation is explained as follows:

$$s = 1 + \frac{4K_B T}{W_H - K_B T \times \ln(\omega\tau_0)} \quad (14)$$

In the modified NSPT model, the temperature $T$ is substituted with $(T - T_0)$, adhering to a VTF form relation. The values of $W_H$, $\tau_0$, and $T_0$ have been derived from the nonlinear curve fitting of experimental data using eqn (14) in Fig. 12, as indicated by the dashed lines. These values are listed in Table 3.

Based on the non-overlapping small polaron tunneling (NSPT) model, the AC conductivity $\sigma_{ac}$ can be determined using the following expression:[68]

$$s = 1 + \frac{4K_B(T - T_0)}{W_H - K_B(T - T_0) \times \ln(\omega\tau_0)} \quad (15)$$

In which $\alpha$ represents the spatial extension of the polaron, $N(E_F)$ denotes the density of defect states, $K_B$ is the Boltzmann constant, $e$ stands for the electronic charge, $\omega$ is the angular frequency, and $R_{T\omega}$ signifies the tunneling distance.

The tunneling distance ($R_{T\omega}$) of small polarons at a fixed frequency ($\omega$) is expressed by:[68]

$$\sigma_{ac} = \frac{(\pi e)^2 K_B T \alpha^{-1} \omega \left[N(E_F)^2\right] {R_{T\omega}}^4}{12} \quad (16)$$

Here $W_H$ is the activation energy for polaron migration, $\alpha$ represents the small polaron wave function in the localized region.

Using eqn (14) for sample values of $T$ in both the lower and higher temperature ranges, the hopping tunneling distance $R_{T\omega}$ is computed. Fig. 14a and b demonstrate that $R_{T\omega}$ rises with increasing temperature and falls with increasing frequency.

The extracted values of $R_{T\omega 1}$ in the lower temperature range are approximately 0.7 Å at a fixed frequency. Higher AC conductivity is linked to this extremely low tunneling distance. On the other hand, the interatomic spacing is equivalent to the recovered values of $R_{T\omega 2}$ in the higher temperature range, which range from 1.2 to 2.3 Å. Thus, it may be concluded that the hopping of tiny polarons between defect states is the main mechanism governing the conduction process.

The density of localized states at the Fermi level, $N(E_F)$, was calculated using eqn (15), assuming an inverse localization length $\alpha^{-1}$ of 1 Å and a fixed frequency of 1 MHz. Fig. 15(a) and (b) illustrate the variation of $N(E_F)$ as a function of frequency at different temperature ranges.

Table 3 Eliott's parameters obtained from eqn (14) and (18)

| | Modified NSPT model | | Modified CBH model | |
|---|---|---|---|---|
| | NSPT I | NSPT II | CBH I | CBH II |
| $w_m$ (eV) | 0.01 | 0.32 | 0.04 | 0.41 |
| $\tau_0$ (s) | $4.15 \times 10^{-5}$ | $5.34 \times 10^{-11}$ | $1.12 \times 10^{-6}$ | $3.99 \times 10^{-11}$ |
| $T_0$ (K) | 273.78 | 544.86 | 276.54 | 289.62 |

As shown, $N(E_F)$ increases with increasing frequency. In the low-temperature region (Fig. 15(a)), $N(E_F)$ also increases with temperature, indicating enhanced thermal activation of charge carriers. In contrast, in the high-temperature region (Fig. 15(b)), $N(E_F)$ decreases as temperature rises, which may be attributed to a reduction in the number of localized states participating in the hopping process due to thermal delocalization effects.

Fig. 14a makes it evident that charge carriers switch from long-distance tunneling to short-distance tunneling at higher frequencies, as the tunneling distance $R_{T\omega 1}$ reduces more quickly as the frequency rises. The increase in $N(E_F)$ with frequency (Fig. 15(a)) can be explained by this tendency.

**3.8.2. Correlated barrier hopping (CBH) model analysis.** The relationship between the polaron binding energy $W_m$ of charge carriers at their localized positions and the power-law exponent $s$ is a characteristic of the CBH model. The following relationship is established for the frequency exponent $s$ by the CBH model:[68]

$$R_{T\omega} = \frac{1}{2\alpha}\left[\mathrm{Ln}\left(\frac{1}{\omega\tau_0}\right) - \frac{W_H}{K_B T}\right] \quad (17)$$

where $K_B$is the Boltzmann constant, $T$ is the absolute temperature, $W_m$ is the binding energy, $\omega$ is the angular frequency, and $\tau_0$ is the characteristic relaxation time.

In this model, thermally activated polarons hop over the potential barrier to neighboring sites.

The CBH model does not satisfactorily fit with experimental results. Consequently, modifications have been made to improve the experimental outcomes. The revised equation for the correlated barrier hopping (CBH) model is presented as follows:[62]

$$s = 1 - \frac{6K_B T}{W_m + K_B T \times \ln(\omega\tau_0)} \quad (18)$$

In the modified CBH model, the temperature $T$ is replaced by $(T - T_0)$ following a VTF type of relation. The values of $W_m$, $\tau_0$, and $T_0$ have been estimated from the nonlinear curve fitting of experimental results using eqn (18) in Fig. 12, as shown by the solid lines. The values are presented in Table 3.

Additionally, according to the CBH model, the AC conductivity can be calculated using the following relation:[68]

$$s = 1 - \frac{6K_B(T - T_0)}{W_m + K_B(T - T_0) \times \ln(\omega\tau_0)} \quad (19)$$

where $n$ represents the number of polarons involved in the hopping process, $N(E_F)$ is the concentration of pair states, and $R_{H\omega}$ is the hopping distance at a specific frequency ($\omega$), as expressed by:[66]

$$\sigma_{ac} = \frac{n\pi^3 \left[N(E_F)^2\right] \varepsilon\varepsilon_0 \omega {R_{H\omega}}^6}{24} \quad (20)$$

The hopping distance $R_{H\omega}$ is evaluated *via* eqn (20) for representative values of $T$ in both lower and higher temperature ranges (II and IV).

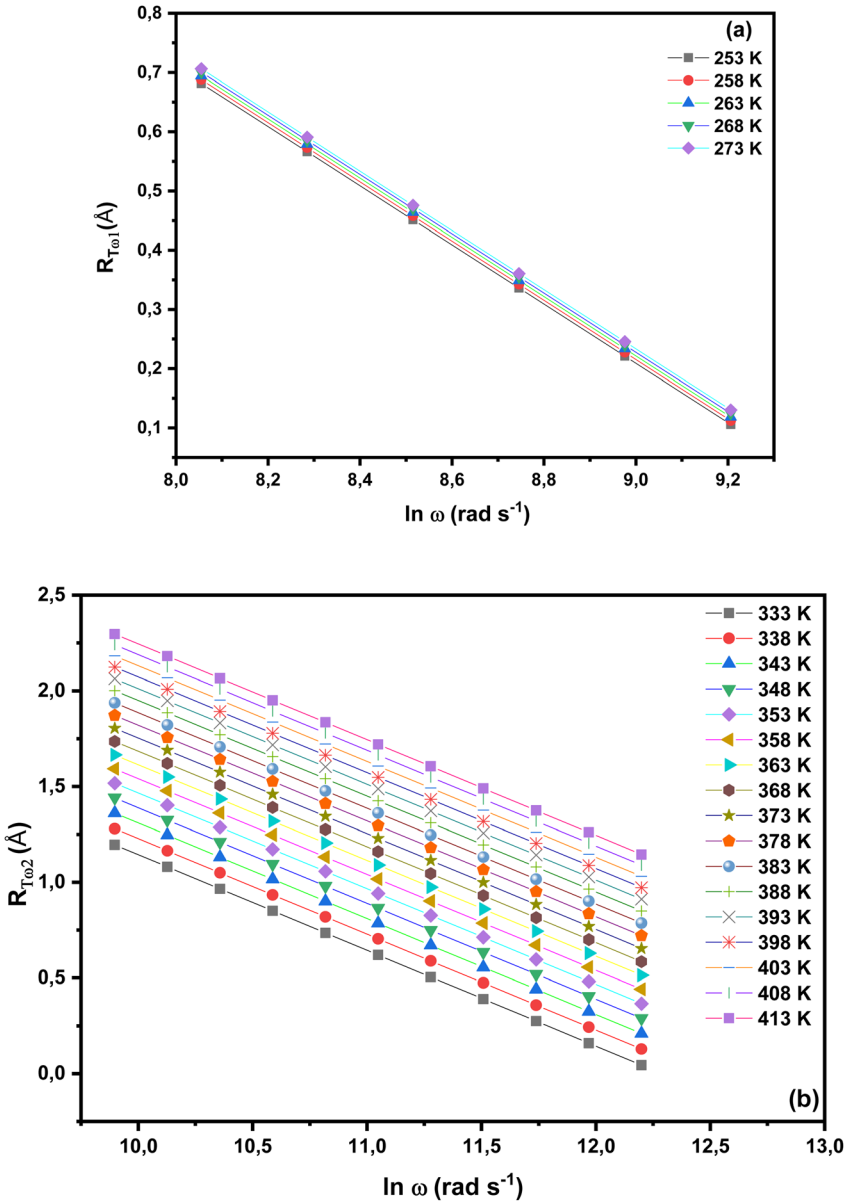


Fig. 14 (a and b) Variation of the tunneling distance $R_{T\omega}$ as a function of frequency at different temperatures for the prepared HAp.

Fig. 16(a) shows that $R_{H\omega 1}$ increases slowly with increasing frequency and rises with temperature. At a fixed frequency, the extracted values of $R_{H\omega 1}$ in the lower temperature range (region II) vary from 0.2 to 4.6 Å. Conversely, Fig. 16(b) indicates that $R_{H\omega 2}$ decreases with both increasing frequency and temperature. At a fixed frequency, the extracted values of $R_{H\omega 2}$ in the higher temperature range (region IV) vary from 2.77 to 3.04 Å. Thus, Fig. 16(a) and (b) shows that the hopping distance $R_{H\omega}$ exhibits two distinct tendencies depending on the temperature range. As shown in the Fig. 16(a), $R_{H\omega 1}$ rises with temperature and, to some degree, with frequency at low and moderate temperatures ($T \leq 318$ K). In this regime, the available thermal energy is still restricted, and only some of the defect states (such as $OH^-$ vacancies or oxygen vacancies) are activated. $R_{H\omega 1}$ gradually rises as a result of carriers having enough energy to go to further localized positions. The small rise of $R_{H\omega 1}$ with frequency in this range further implies that higher frequencies helps carriers overcome the related barriers toward these more faraway states, suggesting a partially activated CBH long-range hopping mechanism. From the Fig. 16(b), the trend for both parameters reverses at higher temperatures ($T > 418$ K). $R_{H\omega 2}$ reduces with rising temperature and also decreases with frequency. The majority of defect states are already accessible in this highly active regime, and the conduction is dominated by quick short-range hops between neighboring sites, which become more effective than long-distance jumps. High frequencies also restrict carrier motion to relatively small distances due to the restricted response time. A shift from thermally enabled long-range hopping at low temperature to a fully active short-range CBH mechanism at high temperature

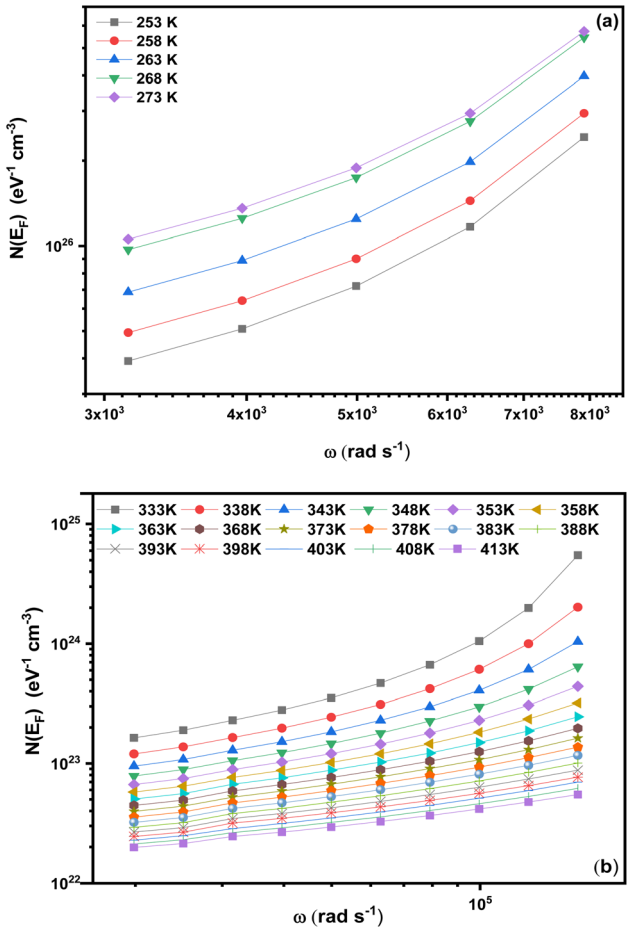


Fig. 15 (a and b) Variation in the localized state density at the Fermi level $N(E_F)$ as a function of frequency at fixed temperatures (region I and III) for the prepared HAp.

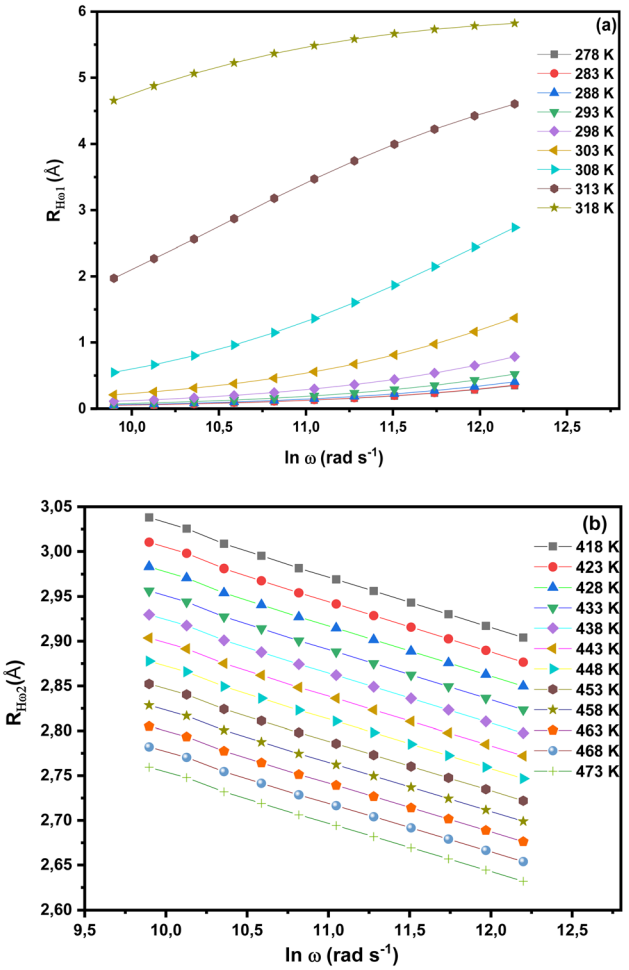


Fig. 16 (a and b) Variation of the hopping distance $R_{H\omega}$ as a function of frequency at different temperatures for the prepared HAp.

is confirmed by the significant decrease in $R_{H\omega 2}$ that results from this.

The localized state density $N(E_F)$ at the Fermi level can be estimated at a constant frequency ($f = 1$ MHz) by using eqn (19). Fig. 17(a and b) depict the variation of $N(E_F)$ as a function of frequency at a fixed temperature.

From these figures, it can be observed that $N(E_F)$ decreases with increasing frequency. In the lower temperature range (region II), $N(E_F)$ decreases with rising temperature (Fig. 17(a)). Conversely, in the higher temperature range (region IV), $N(E_F)$ increases slightly with rising temperature (Fig. 17(b)).

It is also worth mentioning that the particular temperature dependency of the effective number of carriers ($N(E_F)$), notably the increased values obtained at lower temperatures ($10^{28}$ $eV^{-1}$ $cm^{-3}$ at $2 \times 10^4$ Hz and for 278 K), can be explained by the presence of adsorbed water on the surface of hydroxyapatite. Supporting information from FTIR spectra, as well as the activation energy ($E_{dc(a)}$, $E_{dc(b)}$) recovered from $\sigma_{dc}$, supports the coexistence of $H^+$ and $OH^-$ species, demonstrating that a fraction of water molecules remains weakly bonded to the hydroxyapatite surface. At low temperatures, this adsorbed water contributes to an additional number of mobile protons by local dissociation processes, significantly growing the density of charge carriers $N(E_F)$, this effect diminishes between 278 K and 323 K as the adsorbed water gradually desorbs. On the other hand, the removal of surface-adsorbed water and disruption of hydrogen-bond networks cause a small rise in $N(E_F)$ (from $2.2 \times 10^{21}$ to $3 \times 10^{21}$ $eV^{-1}$ $cm^{-3}$ at $2 \times 10^4$ Hz) as temperature rises (from 418 K to 473 K). Accordingly, protonic carriers predominate at low temperatures, while intrinsic ionic carriers of hydroxyapatite predominate at higher temperatures, supporting a mixed conduction mechanism.

### 3.9. Impedance spectroscopy

An ideal Debye-type behavior of the material is usually reflected in the impedance plot, which is mimicked by a parallel RC circuit and features a complete semicircular arc centered on the real axis. Nevertheless, complete Debye behavior is rarely seen in real materials. A constant phase element (CPE) is added to the equivalent circuit in place of an ideal capacitor to account for departures from this ideal response.[69] A dispersion of relaxation times is the source of the CPE behavior. There are two primary kinds of distributions that can happen: (i) a two-dimensional (2D) distribution that is brought on by changes in current or potential along the electrode surface and slow

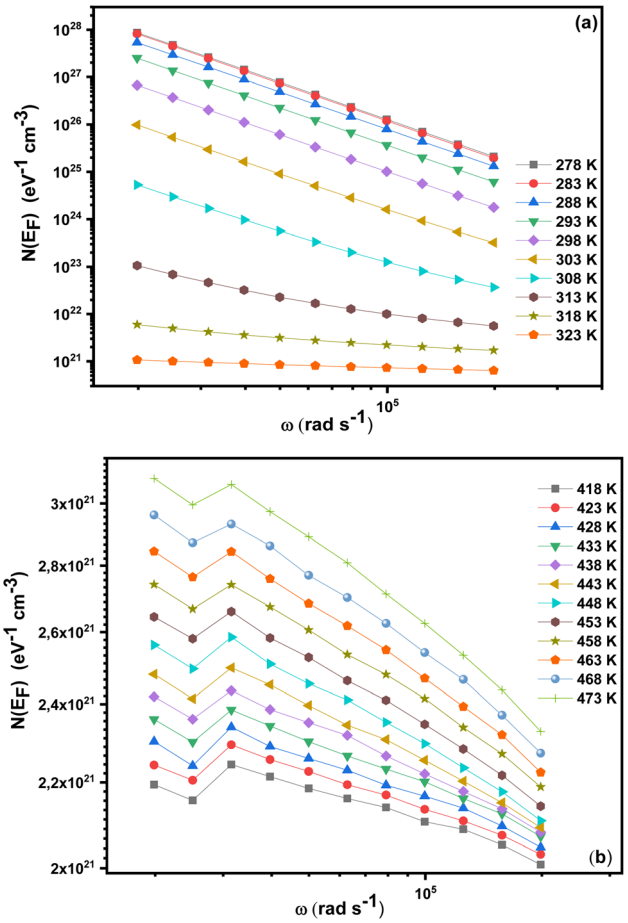


Fig. 17 (a and b) Variation in the localized state density at the Fermi level $N(E_F)$ as a function of frequency at a fixed temperatures (region II and IV) for the prepared HAp.

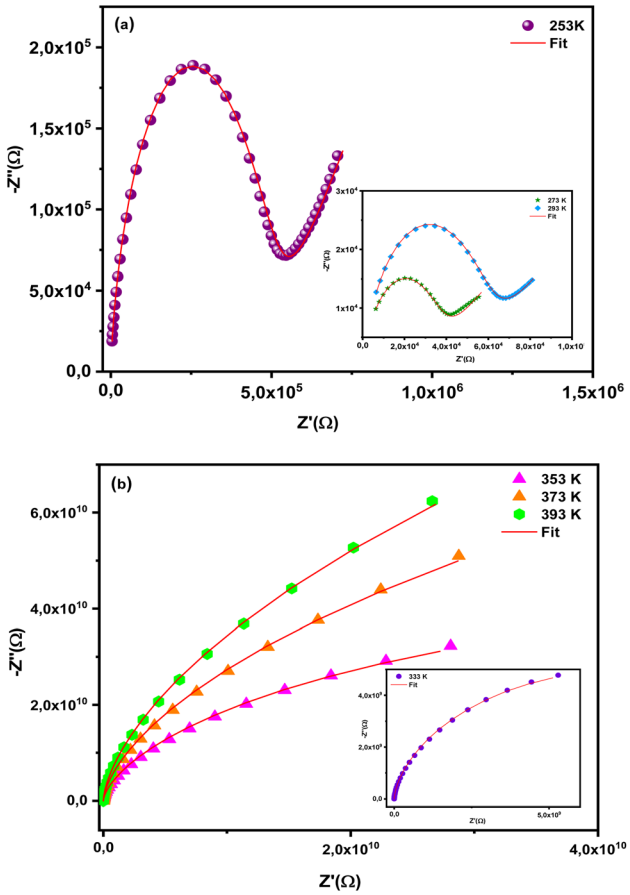


Fig. 18 (a and b) Nyquist plots for the prepared HAp.

kinetics related to charged species adsorption; and (ii) a three-dimensional (3D) distribution that is connected to elements like surface roughness, electrode porosity, and the composition of the heterogeneous coating.[70] Abram *et al.*[71] state that a CPE's impedance can be written as follows:

$$R_{H\omega} = \frac{ne^2}{\pi\varepsilon\varepsilon_0 \left[W_m + K_B T \mathrm{Ln}\omega\tau_0\right]} \quad (21)$$

where $A$ (given by $Z^*_{CPE} = [A_0(j\omega)^n]^{-1}$ with $A$ being a constant referenced in previous studies in previous studies[72]) and $n$ are constants and $j = \sqrt{-1}$. The $Z^*_{CPE}$ is typically regarded as a dispersive capacitance: when $n = 1$, it behaves as an ideal capacitor, whereas when $n = 0$, it acts as a frequency-independent ohmic resistor.

**3.9.1. Nyquist plots and equivalent circuit.** Fig. 18(a and b) shows the hydroxyapatite (HA) sample's complex impedance spectra as Nyquist plots ($Z''$ *vs.* $Z'$) at different temperatures, below and above 313 K, respectively.

The Nyquist plot in Fig. 18(a) reveals a high-frequency semicircle that is prominent and corresponds to bulk properties. This is followed by a lower-frequency semicircle that is linked to space charge effects at the electrode interface. The analogous circuit at temperatures below 313 K is shown in the inset of Fig. 18(a). It is made up of a fractal capacitance (CPE1) and a constant phase element (CPE) connected in series with a bulk resistance ($R_1$). A capacitance C2 is also connected in parallel to this arrangement. Using the *Z*-view software, this analogous circuit was determined to be the best fit and is shown alongside the fitted impedance curves in Fig. 18(a).

A single semicircular arc (or a tendency toward one) may be seen in Fig. 18(b), suggesting that conduction processes mostly take place in the bulk rather than at grain boundaries or surfaces at temperatures higher than 313 K. Additionally, it is clear that both the real and imaginary components of the complex impedance increase when the temperature rises from 313 K to 473 K. According to Nagai *et al.*,[44] this pattern is explained by the sample's water molecules being released at lower temperatures (<473 K), which causes a notable drop in conductivity. The suggested equivalent circuit, which is displayed in the inset of Fig. 18(b), consists of a parallel combination of a real capacitance (C2), fractal capacitance (CPE1), and bulk resistance ($R_1$) for temperatures higher than 313 K. These two parallel capacitances demonstrate how the bulk and grain boundary responses overlap and interact. The optimal equivalent circuit and the fitted impedance curves produced by *Z*-view program are also displayed in Fig. 18(b).

**3.9.2. Analysis of fitted equivalent circuit parameters.** Table 4 and 5 provides a summary of the parameters of the

Table 4 Fitted parameter of the equivalent circuit for the prepared HAp in the temperature range 253 K to 313 K

| $T$ (K) | CPE (μF) | $P$ | $R_1$ (Ω) | CPE1 (nF) | $P_1$ | $C_2$ (pF) |
|---|---|---|---|---|---|---|
| 253 | 0.83064 | 0.31713 | 477 320 | 0.4593 | 0.68377 | 5.7 |
| 258 | 0.98565 | 0.35425 | 278 500 | 0.5297 | 0.68488 | 5.462 |
| 263 | 1.5699 | 0.31548 | 114 010 | 0.4641 | 0.71878 | 5.148 |
| 268 | 1.5637 | 0.35616 | 46 054 | 0.359 | 0.7635 | 3.972 |
| 273 | 3.077 | 0.27417 | 29 945 | 0.3467 | 0.77667 | 4.978 |
| 278 | 2.7582 | 0.32041 | 32 811 | 0.3668 | 0.76846 | 4.093 |
| 283 | 2.8686 | 0.31496 | 34 227 | 0.3237 | 0.77479 | 3.988 |
| 288 | 2.9903 | 0.2835 | 37 720 | 0.2643 | 0.78486 | 4.373 |
| 293 | 2.5949 | 0.27867 | 51 273 | 0.2762 | 0.7702 | 4.729 |
| 298 | 2.0701 | 0.25262 | 79 387 | 0.3016 | 0.74762 | 5.504 |
| 303 | 1.4386 | 0.22687 | 157 710 | 0.4352 | 0.69901 | 6.122 |
| 308 | 0.70373 | 0.22297 | 486 700 | 0.5334 | 0.64733 | 6.319 |
| 313 | 0.2203 | 0.23125 | 2 707 500 | 0.5697 | 0.58345 | 6.39 |

fitted equivalent circuit for the prepared hydroxyapatite (HAp). The fractal capacitance CPE1 reaching values in the nanofarad range at temperatures below 313 K suggests that interfacial effects are important in conduction in the low-temperature area, according to the fitting results shown in Table 4. At these temperatures, increased charge mobility and more uniform surfaces are suggested by the comparatively large fractal capacitance CPE1 and the lowered resistance $R_1$. The data in Table 5 show that resistance $R_1$ increases with temperature, but fractal capacitance CPE1 decreases. Reduced surface conduction brought on by the loss of adsorbed water is the cause of this decrease in CPE1, which moves from the nanofarad to the picofarad region.

Additionally, in accordance with the AC conductivity analysis, the elimination of the CPE component from the analogous circuit at higher temperatures is probably related to a decrease in space charge polarization at the electrodes.

**3.9.3. Activation energy from impedance measurements.** The apparent activation energy related to charge transport through the bulk material was estimated using the DC resistance $R_1$ derived from impedance measurements. A substantial departure from linearity, a sign of non-Arrhenius behavior, is evident in Fig. 19, which shows the fluctuation of the logarithm of the resistance $R_1$ as a function of the inverse absolute temperature (1000/$T$).

Plots of this kind usually produce a straight line (Arrhenius law) in classical conduction processes with a single activation energy. Fig. 19's observed curvature, however, indicates that the electrical conduction mechanism in the synthesized HAp changes with temperature and most likely involves a number of phenomena, including localized charge trapping, interfacial polarization, and thermally assisted hopping. eqn (12), which is derived from the Macedo–Litovitz model, was utilized to fit the experimental data in order to more thoroughly evaluate this phenomenon. The conduction process in disordered materials may be described more precisely thanks to this model, which also takes temperature-dependent relaxation mechanisms into consideration. The resistance $R_1$, which is derived from impedance measurements, accurately depicts the system's temperature-dependent electrical response, as confirmed by the fit quality. Two different temperature regimes are represented by the fitted activation energies, $E_{R(a)}$ and $E_{R(b)}$, respectively: a low-temperature range where charge carrier mobility is more constrained and a high-temperature range where conduction is

Table 5 Fitted parameter of the equivalent circuit for the prepared HAp at temperatures above 313 K

| $T$ (K) | $R_1$ (Ω) | CPE1 (pF) | $P_1$ | CPE2 (pF) | $P_2$ |
|---|---|---|---|---|---|
| 318 | 26 694 000 | 651.3 | 0.46643 | 6.361 | |
| 323 | 480 800 000 | 99.9 | 0.52142 | 6.89 | |
| 328 | 5 341 000 000 | 50.96 | 0.46654 | 6.205 | |
| 333 | $1.877 \times 10^{10}$ | 27.27 | 0.46902 | 6.186 | |
| 338 | $3.943 \times 10^{10}$ | 17.02 | 0.49919 | 6.023 | 1.002 |
| 343 | $7.066 \times 10^{10}$ | 14.04 | 0.47844 | 6.102 | 1.001 |
| 348 | $1.121 \times 10^{11}$ | 12.11 | 0.46153 | 6.156 | 1 |
| 353 | $1.676 \times 10^{11}$ | 10.63 | 0.44732 | 6.196 | 0.99987 |
| 358 | $2.377 \times 10^{11}$ | 9.43 | 0.4364 | 6.225 | 0.99954 |
| 363 | $3.134 \times 10^{11}$ | 8.434 | 0.43072 | 6.243 | 0.99936 |
| 368 | $4.012 \times 10^{11}$ | 7.615 | 0.42576 | 6.257 | 0.9992 |
| 373 | $4.831 \times 10^{11}$ | 6.893 | 0.42467 | 6.276 | 0.99909 |
| 378 | $5.478 \times 10^{11}$ | 6.197 | 0.42772 | 6.272 | 0.99905 |
| 383 | $6.195 \times 10^{11}$ | 5.655 | 0.42992 | 6.276 | 0.99902 |
| 388 | $6.587 \times 10^{11}$ | 5.158 | 0.43577 | 6.278 | 0.99903 |
| 393 | $6.755 \times 10^{11}$ | 4.726 | 0.44488 | 6.274 | 0.99911 |
| 398 | $6.785 \times 10^{11}$ | 4.34 | 0.4559 | 6.27 | 0.9992 |
| 403 | $6.74 \times 10^{11}$ | 4.027 | 0.46737 | 6.26 | 0.99932 |
| 408 | $6.801 \times 10^{11}$ | 3.765 | 0.47774 | 6.254 | 0.99943 |
| 413 | $6.716 \times 10^{11}$ | 3.515 | 0.49175 | 6.241 | 0.999 |
| 418 | $6.752 \times 10^{11}$ | 3.333 | 0.50087 | 6.239 | 0.99971 |
| 423 | $6.886 \times 10^{11}$ | 3.201 | 0.50714 | 6.241 | 0.99969 |
| 428 | $6.954 \times 10^{11}$ | 3.058 | 0.51493 | 6.244 | 0.99968 |
| 433 | $6.995 \times 10^{11}$ | 2.944 | 0.52415 | 6.239 | 0.99976 |
| 438 | $6.736 \times 10^{11}$ | 2.805 | 0.5445 | 6.209 | 1 |
| 443 | $6.536 \times 10^{11}$ | 2.719 | 0.56278 | 6.18 | 1.001 |
| 448 | $6.569 \times 10^{11}$ | 2.643 | 0.57266 | 6.173 | 1.001 |
| 453 | $6.598 \times 10^{11}$ | 2.608 | 0.5786 | 6.173 | 1.001 |
| 458 | $6.638 \times 10^{11}$ | 2.574 | 0.5848 | 6.172 | 1.001 |
| 463 | $6.616 \times 10^{11}$ | 2.546 | 0.59163 | 6.171 | 1.001 |
| 468 | $6.539 \times 10^{11}$ | 2.533 | 0.59753 | 6.171 | 1.001 |
| 473 | $6.481 \times 10^{11}$ | 2.529 | 0.60371 | 6.168 | 1.001 |

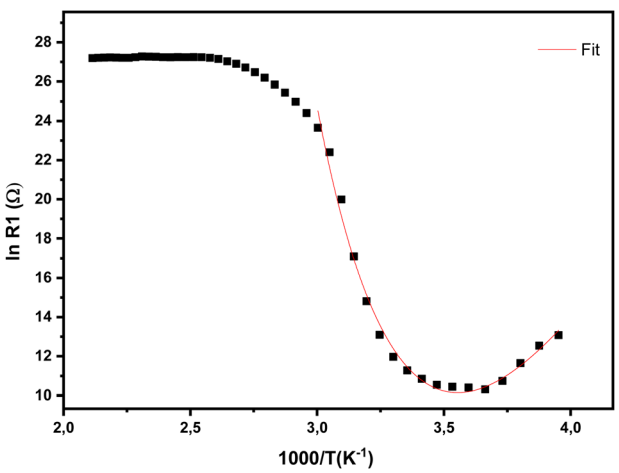


Fig. 19 Logarithmic variation of DC resistance ($R_1$) as a function of the inverse of temperature.

more effective. These values are shown in Table 2 and are in good agreement with the relaxation times ($E_a$, $E_b$) taken from dielectric measurements and the activation energies ($E_{R(a)}$ and $E_{R(b)}$) separately determined from the analysis of DC conductivity. This consistency supports the idea that thermally activated mechanisms that change with temperature control the electrical activity of HAp. Hoping or tunneling between isolated sites predominates at lower temperatures, but the discharge of charge carriers from localized states is probably responsible for the conduction at higher temperatures. The durability of the activation energy values and the dependability of the Macedo–Litovitz model in capturing the intricate conduction dynamics of nanostructured HAp are supported by the good agreement between the various fitting methodologies (DC conductivity, relaxation time, and resistance $R_1$). These results, which are compiled in Table 2, give a thorough overview of the thermally activated processes in the material that was synthesized and shed light on the energy barriers related to charge transport pathways.

## 4. Conclusion

The temperature-dependent AC conductivity of hydroxyapatite (HAp) was thoroughly examined in this work, and Jonscher's and Almond-West's laws were effectively applied to understand the results. Complementary FTIR, DSC, and TGA investigations support the conclusion that the loss of surface-bound water is responsible for the observed drop in conductivity at high temperatures. In line with the concept put out by Macedo and Litovitz, dielectric relaxation phenomena obtained from measurements of the electric modulus ($M''$) and DC conductivity demonstrated pronounced non-Arrhenius behavior. In the low-temperature range (below 473 K), a novel method was used to study this non-Arrhenius conduction behavior. Activation energies derived from $M''$ spectra closely matched those derived from DC conductivity and impedance spectroscopy. A non-Debye relaxation mechanism predominated in the produced HAp samples, according to Nyquist plot analysis. Elliot's theoretical framework was used to further clarify the conduction processes. In regions I and III, the non-overlapping small polaron tunneling (NSPT) model provided a sufficient description of conduction, while in regions II and IV, the correlated barrier hopping (CBH) model did the same. Both models' key parameters were correctly identified. Crucially, for temperatures lower than 473 K, the high agreement between DC conductivity measurements and impedance spectroscopy verifies that the primary cause of the conductivity drop is decreased surface conduction brought on by water molecule desorption. All things considered, this study offers insightful information about the intricate conduction processes in hydroxyapatite, emphasizing the crucial part that surface water and polaron dynamics play in its electrical activity.

## Conflicts of interest

There are no conflicts to declare.

## Data availability

The data supporting the findings of this study are available within the article. Additional data are available from the corresponding author upon reasonable request.

## References

1 G. Dorcioman, V. Grumezescu, G. E. Stan, M. C. Chifiriuc, G. P. Gradisteanu, F. Miculescu, E. Matei, G. Popescu-Pelin, I. Zgura and V. Craciun, *Pharmaceutics*, 2023, **15**, 1294.
2 S. Itoh, S. Nakamura, M. Nakamura, K. Shinomiya and K. Yamashita, *Biomaterials*, 2006, **27**, 5572–5579.
3 T. Kobayashi, S. Nakamura and K. Yamashita, *J. Biomed. Mater. Res.*, 2001, **57**, 477–484.
4 C. Piccirillo and P. M. L. Castro, *J. Environ. Manage.*, 2017, **193**, 79–91.
5 H. Badran, I. S. Yahia, M. S. Hamdy and N. S. Awwad, *Radiat. Phys. Chem.*, 2017, **130**, 85–91.
6 C. Rodríguez-González, H. E. Cid-Luna, P. Salas and V. M. Castaño, *J. Nanomater.*, 2014, **2014**, 940903.
7 D. Kumar, J. P. Gittings, I. G. Turner, C. R. Bowen, A. Bastida-Hidalgo and S. H. Cartmell, *Acta Biomater.*, 2010, **6**, 1549–1554.
8 M. P. Mahabole, R. C. Aiyer, C. V. Ramakrishna, B. Sreedhar and R. S. Khairnar, *Bull. Mater. Sci.*, 2005, **28**, 535–545.
9 N. Horiuchi, M. Nakamura, A. Nagai, K. Katayama and K. Yamashita, *J. Appl. Phys.*, 2012, **112**, 074901.
10 N. A. Zakharov and V. P. Orlovskii, *Tech. Phys. Lett.*, 2001, **27**, 629–631.
11 A. K. Dubey, K. Kakimoto, A. Obata and T. Kasuga, *RSC Adv.*, 2014, **4**, 24601–24611.
12 N. Horiuchi, J. Endo, N. Wada, K. Nozaki, M. Nakamura, A. Nagai, K. Katayama and K. Yamashita, *J. Appl. Phys.*, 2013, **113**, 134905.
13 O. Kaygili, S. V. Dorozhkin, T. Ates, A. A. Al-Ghamdi and F. Yakuphanoglu, *Ceram. Int.*, 2014, **40**, 9395–9402.
14 S. a. W. Pickering and B. E. Scammell, *Int. J. Lower Extremity Wounds*, 2002, **1**, 152–160.
15 P. M. Meaney, T. Zhou, D. Goodwin, A. Golnabi, E. A. Attardo and K. D. Paulsen, *Int. J. Biomed. Imaging*, 2012, **2012**, 1–9.
16 S. Hontsu, T. Matsumoto, J. Ishii, M. Nakamori, H. Tabata and T. Kawai, *Thin solid films*, 1997, **295**, 214–217.
17 S. Itoh, S. Nakamura, T. Kobayashi, K. Shinomiya, K. Yamashita and S. Itoh, *Calcif. Tissue Int.*, 2006, **78**, 133–142.
18 K. Yamashita, N. Oikawa and T. Umegaki, *Chem. Mater.*, 1996, **8**, 2697–2700.
19 M. Nakamura, A. Nagai, N. Ohashi, Y. Tanaka, Y. Sekijima, S. Nakamura and K. Yamashita, *Key Eng. Mater.*, 2008, **361**, 1055–1058.
20 H. Ivankovic, E. Tkalcec, S. Orlic, G. Gallego Ferrer and Z. Schauperl, *J. Mater. Sci.: Mater. Med.*, 2010, **21**, 2711–2722.
21 J. I. Langford and A. J. C. Wilson, *Appl. Crystallogr.*, 1978, **11**, 102–113.
22 L. V. Azaroff, *Elements of X-ray Crystallography*, 1968.
23 E. Landi, A. Tampieri, G. Celotti and S. Sprio, *J. Eur. Ceram. Soc.*, 2000, **20**, 2377–2387.

24 N. Zhanglei, Z. CHANG, L. I. Wenjun, S. Changyan, J. ZHANG and L. Yang, *Chin. J. Chem. Eng.*, 2012, **20**, 89–94.
25 R. V. Suganthi, K. Elayaraja, M. A. Joshy, V. S. Chandra, E. K. Girija and S. N. Kalkura, *Mater. Sci. Eng. C*, 2011, **31**, 593–599.
26 A. Yelten-Yilmaz and S. Yilmaz, *Ceram. Int.*, 2018, **44**, 9703–9710.
27 M. C. Chang and J. Tanaka, *Biomaterials*, 2002, **23**, 4811–4818.
28 H. El Feki, J. M. Savariault and A. B. Salah, *J. Alloys Compd.*, 1999, **287**, 114–120.
29 E. Landi, G. Celotti, G. Logroscino and A. Tampieri, *J. Eur. Ceram. Soc.*, 2003, **23**, 2931–2937.
30 S. S. A. Abidi and Q. Murtaza, *J. Mater. Sci. Technol.*, 2014, **30**, 307–310.
31 M. Boutinguiza, J. Pou, R. Comesaña, F. Lusquiños, A. de Carlos and B. León, *Mater. Sci. Eng. C*, 2012, **32**, 478–486.
32 H. K. Varma and S. S. Babu, *Ceram. Int.*, 2005, **31**, 109–114.
33 A. Paz, D. Guadarrama, M. López, J. E González, N. Brizuela and J. Aragón, *Quim. Nova*, 2012, **35**, 1724–1727.
34 J. D. Pasteris, B. Wopenka, J. J. Freeman, K. Rogers, E. Valsami-Jones, J. A. Van der Houwen and M. J. Silva, *Biomaterials*, 2004, **25**, 229–238.
35 M. Irfan, P. S. Suprajaa, R. Praveen and B. M. Reddy, *Mater. Lett.*, 2021, **282**, 128685.
36 K. Tõnsuaadu, K. A. Gross, L. Plūduma and M. Veiderma, *J. Therm. Anal. Calorim.*, 2012, **110**, 647–659.
37 C.-J. Liao, F.-H. Lin, K.-S. Chen and J.-S. Sun, *Biomaterials*, 1999, **20**, 1807–1813.
38 H. Tanaka, M. Chikazawa, K. Kandori and T. Ishikawa, *Phys. Chem. Chem. Phys.*, 2000, **2**, 2647–2650.
39 D. P. Almond, G. K. Duncan and A. R. West, *Solid State Ionics*, 1983, **8**, 159–164.
40 M. Hema, S. Selvasekerapandian, G. Hirankumar, A. Sakunthala, D. Arunkumar and H. Nithya, *J. Phys. Chem. Solids*, 2009, **70**, 1098–1103.
41 A. K. Jonscher, *J. Phys. D: Appl. Phys.*, 1999, **32**, R57.
42 J. P. Gittings, C. R. Bowen, A. C. Dent, I. G. Turner, F. R. Baxter and J. B. Chaudhuri, *Acta Biomater.*, 2009, **5**, 743–754.
43 P. K. Roy, V. Kalia and J. Bera, *Comparison of Electrical Properties between Ca and Sr Hydroxyapatites Materials*, 2004.
44 M. Nagai and T. Nishino, *Solid State Ionics*, 1988, **28**, 1456–1461.
45 K. Yamashita, K. Kitagaki and T. Umegaki, *J. Am. Ceram. Soc.*, 1995, **78**, 1191–1197.
46 Y. Tanaka, M. Nakamura, A. Nagai, T. Toyama and K. Yamashita, *Mater. Sci. Eng. B*, 2009, **161**, 115–119.
47 J. Tauke, T. A. Litovitz and P. B. Macedo, *J. Am. Ceram. Soc.*, 1968, **51**, 158–163.
48 T. S. Ree, T. Ree and H. Eyring, *Proc. Natl. Acad. Sci. U. S. A*, 1962, **48**, 501–517.
49 G. Adam and J. H. Gibbs, *J. Chem. Phys.*, 1965, **43**, 139–146.
50 D. B. Davies and A. J. Matheson, *J. Chem. Phys.*, 1966, **45**, 1000–1006.
51 P. B. Macedo and T. A. Litovitz, *J. Chem. Phys.*, 1965, **42**, 245–256.
52 H. Douiri, I. Kaddoussi, S. Baklouti, M. Arous and Z. Fakhfakh, *J. Non-Cryst. Solids*, 2016, **445**, 95–101.
53 D. P. Almond and A. R. West, *Nature*, 1983, **306**, 456–457.
54 M. S. Khalil, H. H. Beheri and W. I. A. Fattah, *Ceram. Int.*, 2002, **28**, 451–458.
55 B. S. H. Royce, *Ann. N. Y. Acad. Sci.*, 1974, **238**, 131–138.
56 A. Das and D. Pamu, *Mater. Sci. Eng. C*, 2019, **101**, 539–563.
57 N. Horiuchi, S. Nakaguki, N. Wada, K. Nozaki, M. Nakamura, A. Nagai, K. Katayama and K. Yamashita, *J. Appl. Phys.*, 2014, **116**, 014902.
58 C. Yoder, J. Pasteris, K. Worcester, D. Schermerhorn, M. Sternlieb, J. Goldenberg and Z. Wilt, *Minerals*, 2012, **2**, 100–117.
59 T. Chatterjee, A. K. Das, S. Lala, S. K. Pradhan and A. K. Meikap, *J. Appl. Phys.*, 2019, **125**, 225107.
60 T. Wei, Z. Dong, C. Z. Zhao, Y. Y. Guo, Q. J. Zhou and Z. P. Li, *J. Appl. Phys.*, 2016, **119**, 124107.
61 J. Liu, C.-G. Duan, W.-G. Yin, W.-N. Mei, R. W. Smith and J. R. Hardy, *J. Chem. Phys.*, 2003, **119**, 2812–2819.
62 S. Bhattacharya and A. Acharya, in *Metal Oxide Glass Nanocomposites*, Elsevier, 2020, pp. 189–206.
63 A. Ghosh and D. Chakravorty, *J. Phys.: Condens. Matter*, 1990, **2**, 5365.
64 X. Le Cleac'h, *J. Phys.*, 1979, **40**, 417–428.
65 G. E. Pike, *Phys. Rev. B: Condens. Matter Mater. Phys.*, 1972, **6**, 1572–1580.
66 S. R. Elliott, *Philos. Mag.*, 1977, **36**, 1291–1304.
67 N. F. Mott and E. A. Davis, *Electronic Processes in Non-crystalline Materials*, Oxford University Press, 2012.
68 A. R. Long, *Adv. Phys.*, 1982, **31**, 553–637.
69 A. R. West, D. C. Sinclair and N. Hirose, *J. Electroceram.*, 1997, **1**, 65–71.
70 J.-B. Jorcin, M. E. Orazem, N. Pébère and B. Tribollet, *Electrochim. Acta*, 2006, **51**, 1473–1479.
71 E. J. Abram, D. C. Sinclair and A. R. West, *J. Electroceram.*, 2003, **10**, 165–177.
72 D. P. Almond and A. R. West, *Solid State Ionics*, 1983, **9**, 277–282.